

# Effect of Immersion Routes on the Quenching Distortion of a Long Steel Component Using a Finite Element Model

R. D. Lopez-Garcia<sup>1</sup>  · F. A. Garcia-Pastor<sup>1</sup> · M. J. Castro-Roman<sup>1</sup> · E. Alfaro-Lopez<sup>2</sup> · F. A. Acosta-Gonzalez<sup>1</sup>

Received: 9 May 2015 / Accepted: 13 October 2015 / Published online: 12 February 2016  
© The Indian Institute of Metals - IIM 2016

**Abstract** Distortion while quenching steel is a commonly found problem in industrial practice. This issue arises from the combined effect of thermal contraction and martensite transformation stresses. This problem may be exacerbated in components with long geometries. This work presents the results of a numerical and experimental investigation that assessed the effect of both the austenite grain size (AGS) of three sizes 8, 9 and 10 ASTM, and the immersion route on the distortion of a long component of SAE 5160 steel during oil quenching. The transformation kinetics were calculated using JMatPro and were validated by quench dilatometry. A three-dimensional finite element model was developed in Deform 3D. This model was then validated using thermocouple data. Results showed that the distortion was minimized when the long component was dipped sideways in the quenching medium instead of immersing the component from the distal ends when the AGS was 8 ASTM.

**Keywords** FEM · Steel · Quenching · Distortion

## 1 Introduction

Quenching is one of the most widely applied heat treatments in steel processing to improve mechanical properties such as strength and hardness. Mathematical modeling is one of several tools being used to further understand the interactions that occur during quenching [1–8]. In this process, components are cooled rapidly using cooling media, such as air, water, brine or oil to avoid diffusion controlled transformations in favor of the adiffusional martensite transformation. There is a critical cooling rate which is required to suppress the diffusion transformations such as austenite-pearlite and austenite-bainite, which is a function of alloy chemistry and AGS [9, 10]. The formation of bainite is undesirable in traditional quenching processes because this phase is not as hard as martensite and subsequent tempering processes may be affected by its presence [11, 12]. In components which require superior dimensional controls, such as automotive and aerospace components, distortion during quenching may be an important problem. It is accepted that distortion is caused by the combined effect of thermal and martensite transformation stresses [13–18]. Among other mathematical tools, finite element method (FEM) modeling has been used for further understanding of the quenching parameters and the effects they may have on distortion [2–5, 7, 19–24].

One of the most difficult issues to develop an accurate distortion model is the determination of a heat transfer coefficient (HTC) at the quenching interface. This HTC is a function of the part surface and quenching media temperature, as well as the media agitation [19, 25–28]. Distortion may be more likely in components with complex

---

✉ R. D. Lopez-Garcia  
rdlgitecv@hotmail.com; r.lopez@microestructura.org

✉ F. A. Garcia-Pastor  
francisco.garcia@cinvestav.edu.mx

M. J. Castro-Roman  
manuel.castro@cinvestav.edu.mx

E. Alfaro-Lopez  
ealfarol@rassini.com

F. A. Acosta-Gonzalez  
andres.acosta@cinvestav.edu.mx

<sup>1</sup> Cinvestav Unidad Saltillo, Av. Industria Metalúrgica No. 1062. Parque Industrial, Ramos Arizpe, Coahuila, Mexico

<sup>2</sup> San Luis Rassini, Puerto Arturo 803, Col. Bravo, Piedras Negras, Coahuila, Mexico

geometries, in particular the so-called long geometries, with a length:width ratio over 7. Additional parameters, such as dipping route, and inhomogeneous heat extraction have also been reported to have roles in distortion [29–32]. Among industrial components commonly affected by distortion, automotive leaf springs manufactured from steel strips are an important example, both in terms of geometry and dimensional strict controls.

In this work the effect of both the AGS and the oil-quenching route on the distortion of a long steel component were assessed using a numerical FEM approach based on experimental data. Macroscopic distortion was analyzed both dimensionally and in terms of the evolution of the martensite volume fraction distribution along the whole component volume. HTC was calculated from experimental data. JMatPro was used to calculate transformation kinetics which were later refined using quench dilatometry. A fully coupled three-dimensional FEM model with the previously calculated HTC and transformation kinetics was developed using the commercial software Deform 3D.

## 1.1 Modeling

During the last three decades, several heat treatment processes have been simulated by numerical methods. Specifically, quenching has been simulated using mostly FEM software [33]. The FEM is a computational technique used to obtain approximate solutions of boundary value problems in engineering. Usually, FEM divides the definition domain into reasonably defined subdomains (elements) by hypothesis and supposes that the unknown state variables' function in each element, is approximately defined. Thus the approximate solutions of the boundary value and initial value problems are obtained. Considering the complex phenomena occurring during quenching, it is understandable that why FEM approaches are preferred to simulate this heat treatment process. In fact, it is possible to find several commercial FEM software suites capable of simulating the quenching process, such as DANTE, DEFORM-HT, FORGE, HEARTS and TRAST [34].

Quenching is a multi-physics process involving a complicated pattern of couplings between different physical events such as heat transfer, phase transformations, and stress evolution. Based on the above, several works based on FEM have been developed, in order to gain and improve knowledge on: heat transfer, phase transformations, mechanics of materials, fluid dynamics, and numerical methods for computer implementation of problems [3, 4, 10, 35–38].

The computer simulation of the quenching process includes three main parts: heat transfer, phase

transformations, and deformation due to temperature and phase changes. It has been reported that, martensitic phase transformation in steels has a larger contribution on stress generation and distortion than the thermal gradients during the quenching process [3, 37].

Quenching can be defined as a transient heat conduction problem with convective and radiation boundary conditions with internal heat source and sink. The governing equation for this problem has been formulated by Fourier's law:

$$q = -k\nabla T \quad (1)$$

where  $q$  is the vector of heat flow per unit area,  $k$  is thermal conductivity and  $\nabla T$  is the gradient of the temperature field inside the material.

### 1.1.1 Thermal Modeling

According to the Fourier law, the Fourier heat conduction equation of transient problem with the phase-transformation latent heat can be achieved by using conservation of energy in a rectangular coordinates system. The equation can be written as:

$$\frac{\partial}{\partial x} \left( k \frac{\partial T}{\partial x} \right) + \frac{\partial}{\partial y} \left( k \frac{\partial T}{\partial y} \right) + \frac{\partial}{\partial z} \left( k \frac{\partial T}{\partial z} \right) + q_v = \left( \frac{\partial T}{\partial t} \rho C_p \right) \quad (2)$$

where  $k$  is the thermal conductivity,  $T$  is the temperature of the quenching part,  $q_v$  is the rate of heat generation from the steel phase transformation,  $\rho$  is the density of material,  $C_p$  is the specific heat constant pressure,  $t$  is the time,  $x$ ,  $y$  and  $z$ , are the rectangular coordinates. The boundary condition of heat transfer is:

$$k \frac{\partial T}{\partial n} \Big|_{\Gamma} = h(T)(T_{\infty} - T_a) \quad (3)$$

where  $n$  is the normal direction to the solid surface,  $h(T)$  is the heat transfer coefficient (HTC) at the surface  $\Gamma$ , which is a function of temperature, and is determined from the measured temperature evolution data which have been analyzed with the solution of the Inverse Heat Conduction Problem (IHCP) [39].  $T_a$  and  $T_{\infty}$  denote the instantaneous surface temperature of the part and the temperature of the quenching media, respectively. The rate of heat transmission by convection and radiation between the surface of the solid component and the fluid quenching medium can be calculated using Newton's equation of cooling:

$$Q = hA\Delta T \quad (4)$$

where  $Q$  is the heat flux,  $h$  is the heat-transfer coefficient which combines the influence of the convection and radiation,  $A$  is the surface area of the solid component, and  $\Delta T$

is the temperature difference between the surface of the component and the quenching medium.

### 1.1.2 Modeling of Phase Transformation

A time–temperature–transformation (TTT) diagram describes the relationship between the starting and ending of transformation, and the transformed volume fraction during the isothermal process at different temperatures. The isothermal kinetic equation, namely Johnson-Mehl equation [40], provides a solid base for numerical simulation of thermal processes, although it cannot be directly applied to calculate the volume fraction during non-isothermal processes, such as industrial heating or cooling treatments. Due to the strict limitation of Johnson-Mehl equation, Avrami [41] proposed an empirical equation, which has a simpler form and has been widely used, as follows:

$$f = 1 - \exp(-bt^n) \tag{5}$$

where  $f$  is the volume fraction of a new phase,  $t$  is the isothermal time duration,  $b$  is a constant dependent on the temperature, composition of parent phase, and the grain size and  $n$  is also a constant dependent on the type of phase transformation and ranges from 1 to 4.

Coefficients  $b$  and  $n$  at different temperatures are usually calculated from the experimentally obtained TTT diagram by the following equations:

$$n = \frac{\ln[\ln(1 - f_1) - \ln(1 - f_2)]}{\ln t_1 - \ln t_2}$$

$$b = - \left[ \frac{\ln(1 - f_1)}{t_1^n} \right] \tag{6}$$

$b$  depends on temperature according to Arrhenius type equation given by the expression:

$$b = b_0 \exp\left(\frac{-Q}{RT}\right) \tag{7}$$

where  $b_0$  is the frequency factor,  $Q$  is the activation energy for the transformation,  $R$  is the gas constant and  $T$  is absolute temperature.

**1.1.2.1 Martensitic Transformation** Martensite is commonly considered to form by a time-independent transformation below  $M_s$  temperature [42]. Physically, there exists a nucleation and growth stage, but the growth rate is

so high that the rate of volume transformation is almost entirely controlled by nucleation. In fact, the austenite–martensite interface moves almost at the speed of sound in the solid. Therefore, its kinetics is essentially not influenced by the cooling rate and cannot be described by Avrami type of kinetic equations. The amount of martensite formed is often calculated as a function of temperature using the law established by Koistinen and Marburger [42]:

$$V = 1 - \exp[-\alpha(M_s - T)] \tag{8}$$

where  $V$  is the transformed volume fraction of martensite,  $T$  is the temperature,  $M_s$  is the start temperature of martensitic transformation and  $\alpha$  is the constant reflecting the transformation rate and depends on the steel composition. For carbon steel with carbon lower than 1.1 %, we have  $\alpha = 0.011$ .

## 2 Experimental Procedure

Table 1 shows the chemical composition of the SAE 5160 steel used in this study, commonly used in spring applications. The analyzed component measured 1500 mm long, 60 mm wide and 10 mm thick, a typical leaf spring dimensions. The computational domain representing this component is presented in Fig. 1.

To analyze the macroscopic distortion and calculate the heat transfer coefficient, our full component of SAE 5160 steel was instrumented with K-type thermocouples located in the center of the component, as indicated in Fig. 1. One was welded to the surface and the other was tightly inserted upto 5 mm from the surface. This component was austenitized for 11 min at 920 °C and quenched in oil at 60 °C at Rassini’s facilities. The quenching tank was used in production and agitated in the first half of the dipping section, with a baffle limiting the agitation in the second half. The component was submerged for 90 s. The thermal data were recorded using a computerized acquisition system. The HTC was fitted using the thermal history data thus obtained. Final martensite volume fraction was measured using common metallography techniques. Finally, a saturated picric acid solution was used to reveal the austenite grain size prior to quenching.

JMatPro was used to calculate the transformation kinetics and martensite linear expansion. These initial calculations were further refined with data obtained from a

**Table 1** Chemical composition of SAE 5160 steel

Element	C	Mn	Cr	Si	Cu	Ni	Fe
(wt%)	0.6	0.87	0.96	0.25	0.22	0.14	Balance

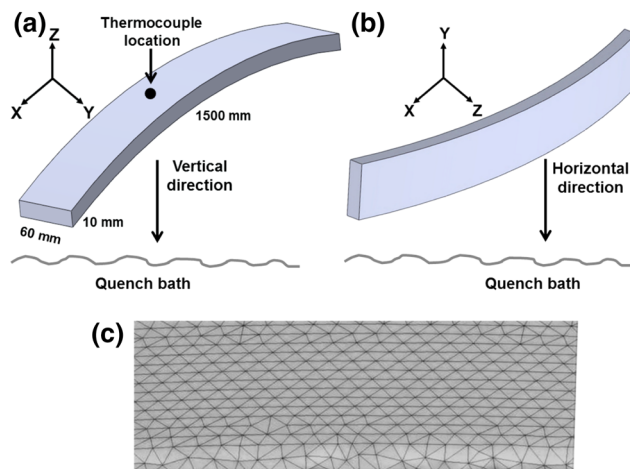


**Fig. 1** Computational domain used in the simulation showing dipping trajectories. **a** vertical, in Z direction, i.e. from the ends, **b** horizontal, in Y direction, i.e. from the edge and **c** meshing the component geometry

quench dilatometer (L78 RITA Linseis Messgeräte, Germany). Induction heating and helium cooling were used in the experimental setup, with a cylindrical sample (10 mm long and 3 mm thick) instrumented with a k-type thermocouple recording 1000 data points per second. Data for AGS of 8, 9 and 10 ASTM were obtained and TTT diagrams were constructed from isothermal holding following different cooling routes.

## 2.1 FEM simulation Procedure and Input Data

Deform 3D (Scientific Forming Technology Corporation, Columbus, Ohio, USA) was used to develop the fully coupled model, following the equations described previously [43]. Most physical properties were obtained from Deform 3D database, while transformation kinetics were determined as described in the previous paragraphs.

Using data from the instrumented component as described in the previous section, the interfacial HTC was determined using the solution to the IHCP, implemented in the CONTA code. The HTC thus obtained represented an improvement over previously reported constant values as well as other variable values, since each quenching setup had particular parameter which might affect heat transfer at the component-media interface [4]. Table 2 summarizes the simulation parameters used. The computational mesh was comprised of approximately 100,000 elements as shown in Fig. 1. This allowed to obtain results that were independent of the mesh itself. In order to analyze the effect of immersion route on quenching distortion, the defined computational domain was dipped into a parallelepiped volume representing the quenching pool. The code DEFORM has the capability to introduce a solid

**Table 2** Simulation parameters

Simulation parameters	Value(s)
Poisson's ratio	0.3
Iteration method	Newton–Raphson
Thermal conductivity	$k$ (determined for each phase)
Heat transfer coefficient	$f(T)$ , shown in Fig. 3
Number of simulation steps	900
Number of elements	100,000
Number of nodes	14,156
Initial temperature (°C)	920
Environment temperature (°C)	50
Quenching oil temperature (°C)	60
Immersion speed (mm/s)	40
Dipping direction	Z and Y
Austenite grain size (ASTM)	8, 9 and 10

object into a pool at a given speed. Basically this is done by sequentially switching on the oil cooling boundary condition through the surface of the object, as if it were immersed in a pool. The immersion speed in both cases was 40 mm/s. Figure 1 shows the two different quenching routes that were simulated, (1) from the ends, following common industrial practice, and (2) from the edge.

The initial temperature was set to 920 °C for all the nodes and all the elements were assumed to be made up of 100 % homogeneous austenite with a defined grain size. The austenitizing heat treatment of the components as well as their hot working were simulated to obtain the final shape. Distortion and residual stresses generated during those previous processes were considered at the beginning of the simulation, and were found to be negligible.

Thermal and mechanical properties such as specific heat ( $C_p$ ), thermal conductivity ( $k$ ), enthalpy ( $H$ ), density ( $\rho$ ), Young's modulus ( $E$ ), Poisson ratio ( $\nu$ ), flow stress ( $S_f$ ), and yield stress ( $S_y$ ) of the material were defined to be dependent on the current phase.

The element properties were computed as a sum of the contributions of the individual fractions of phases present in the element at the particular time step. The properties of individual phases were obtained using JMatPro [44]. These properties for a grain size of 8 ASTM are shown in Tables 3, 4 and 5.

## 3 Results and Discussion

### 3.1 Heat Transfer Coefficient Calculations

The curve-fitting between the calculated and measured surface temperature values is depicted in Fig. 2. The average difference between the measured and computed

**Table 3** Material data for SAE 5160 steel (austenite phase)

T (°C)	$C_p$ J/(Kg °C)	$k$ W/(m °C)	H (J/Kg)	$\rho$ (kg/m <sup>3</sup> )	E (GPa)	$\nu$	$S_f$ (MPa)	$S_y$ (MPa)
25	$4.53 \times 10^5$	17.1	$1.51 \times 10^5$	$8.03 \times 10^3$	199.7	0.292	3353.1	312.1
100	$4.76 \times 10^5$	18.1	$1.86 \times 10^5$	$7.99 \times 10^3$	193.2	0.297	3106.6	261.8
200	$4.99 \times 10^5$	19.2	$2.35 \times 10^5$	$7.94 \times 10^3$	184.4	0.302	2924.4	226.8
300	$5.18 \times 10^5$	20.5	$2.86 \times 10^5$	$7.88 \times 10^3$	175.5	0.308	2817.1	207.1
400	$5.35 \times 10^5$	21.7	$3.39 \times 10^5$	$7.82 \times 10^3$	166.5	0.314	2746.2	194.5
500	$5.52 \times 10^5$	22.9	$3.93 \times 10^5$	$7.77 \times 10^3$	157.3	0.320	856.3	185.7
600	$5.68 \times 10^5$	24.1	$4.49 \times 10^5$	$7.71 \times 10^3$	148.1	0.326	328.1	179.3
700	$5.84 \times 10^5$	25.3	$5.07 \times 10^5$	$7.66 \times 10^3$	138.6	0.331	118.6	174.5
800	$6.01 \times 10^5$	26.5	$5.66 \times 10^5$	$7.60 \times 10^3$	129.1	0.337	85.5	170.6
900	$6.15 \times 10^5$	27.7	$6.27 \times 10^5$	$7.55 \times 10^3$	119.4	0.343	50.3	167.5

**Table 4** Material data for SAE 5160 steel (bainite and pearlite phases)

T (°C)	$C_p$ J/(Kg °C)	$k$ W/(m °C)	H (J/Kg)	$\rho$ (kg/m <sup>3</sup> )	E (GPa)	$\nu$	$S_f$ (MPa)	$S_y$ (MPa)
25	$4.62 \times 10^5$	42.7	0	$7.82 \times 10^3$	210.3	0.287	3353.1	1056.2
100	$4.91 \times 10^5$	42.2	$3.39 \times 10^4$	$7.80 \times 10^3$	206.9	0.290	3106.6	923.5
200	$5.28 \times 10^5$	40.9	$8.48 \times 10^4$	$7.77 \times 10^3$	201.2	0.294	2924.4	831.2
300	$5.69 \times 10^5$	39.1	$1.39 \times 10^5$	$7.73 \times 10^3$	193.5	0.297	2817.1	779.2
400	$6.19 \times 10^5$	36.9	$2.24 \times 10^5$	$7.70 \times 10^3$	184.1	0.301	2746.2	745.9
500	$6.83 \times 10^5$	34.7	$2.64 \times 10^5$	$7.67 \times 10^3$	172.9	0.304	856.3	717.6
600	$7.93 \times 10^5$	–	$3.37 \times 10^5$	–	–	–	328.1	–
700	$9.45 \times 10^5$	–	$4.23 \times 10^5$	–	–	–	118.6	–
800	$8.45 \times 10^5$	–	$5.18 \times 10^5$	–	–	–	85.5	–
900	$7.83 \times 10^5$	–	$5.99 \times 10^5$	–	–	–	50.3	–

**Table 5** Material data for SAE 5160 steel (martensite phase)

T (°C)	$C_p$ J/(Kg °C)	$k$ W/(m °C)	H (J/Kg)	$\rho$ (Kg/m <sup>3</sup> )	E (GPa)	$\nu$	$S_f$ (MPa)	$S_y$ (MPa)
25	$4.88 \times 10^5$	35.5	$5.12 \times 10^4$	$7.77 \times 10^3$	209.9	0.289	3353.1	2128.4
50	$4.59 \times 10^5$	36.2	$6.25 \times 10^4$	$7.76 \times 10^3$	208.9	0.290	3253.6	2025.5
100	$4.80 \times 10^5$	37.3	$8.61 \times 10^4$	$7.74 \times 10^3$	206.6	0.292	3106.6	1877.1
150	$5.00 \times 10^5$	38.1	$1.10 \times 10^5$	$7.73 \times 10^3$	203.9	0.294	3001.9	1775.6
200	$5.21 \times 10^5$	38.6	$1.36 \times 10^5$	$7.71 \times 10^3$	200.7	0.296	2924.4	1702.2
250	$5.44 \times 10^5$	38.8	$1.62 \times 10^5$	$7.69 \times 10^3$	197.1	0.298	2864.6	1646.8

temperatures by the IHCP is 3.57 % thus showing an excellent agreement. The computed heat flux at the surface and corresponding HTC are presented in Fig. 3 as a function of surface temperature.

First, the HTC increases during cooling since the vapor film, formed at high temperature, starts breaking at lower surface temperatures and then the HTC reaches a

maximum. At approximately 450 °C, the HTC decreases fast with further cooling, because it enters into the nucleate boiling regime. In this regime, the rate of oil boiling decreases because the surface temperature approaches to the boiling point of the oil ( $T_{sat} = 280\text{--}300$  °C), leading to a decrease in the heat transfer coefficient. Below 280 °C, steel transforms into martensite and releases the

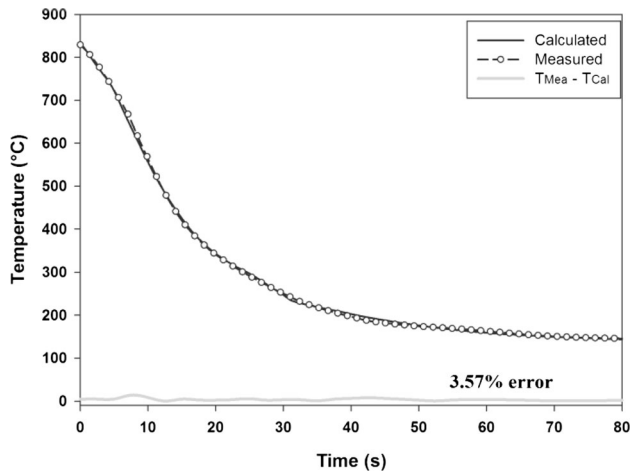


**Fig. 2** Surface temperature fitting between calculated and measured values

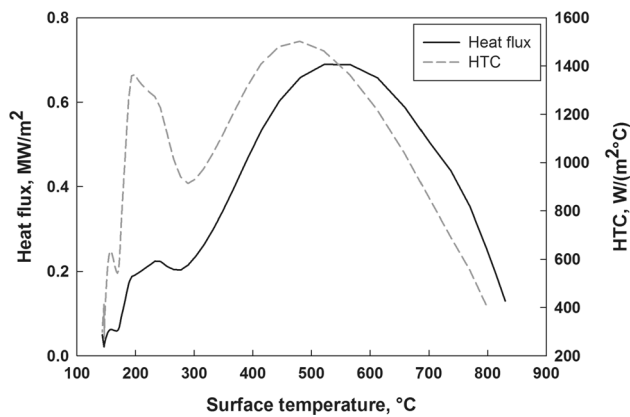


**Fig. 3** Heat transfer coefficient (HTC) and heat flux as a function of surface temperature of the component

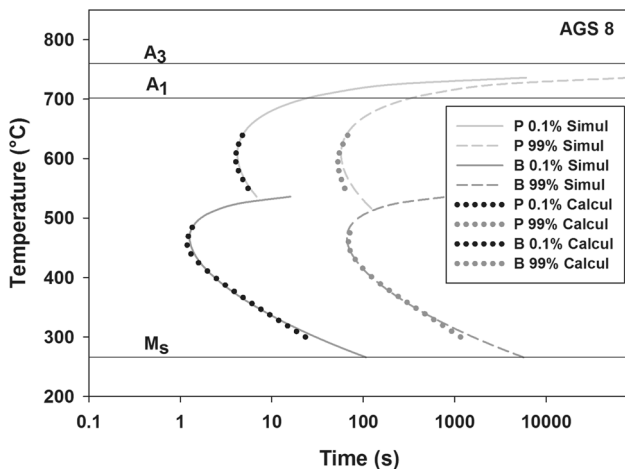


**Fig. 4** TTT diagram of the transformation kinetics of pearlite and bainite for austenitic grain size AGS 8

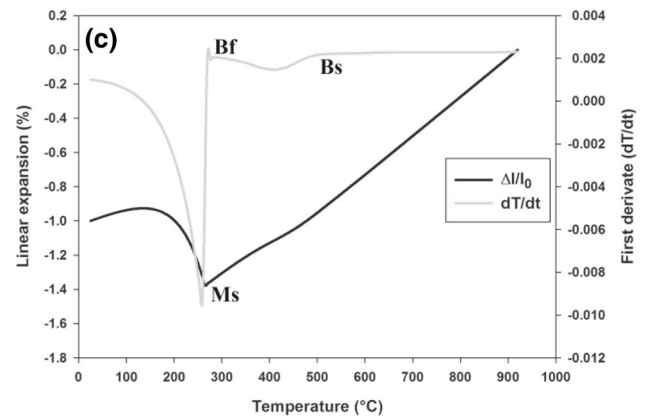
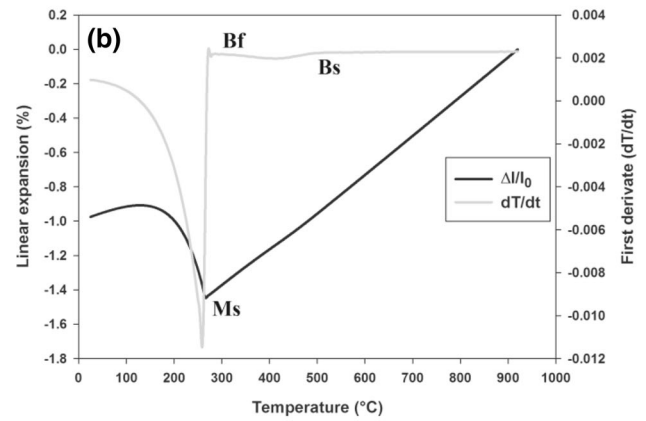
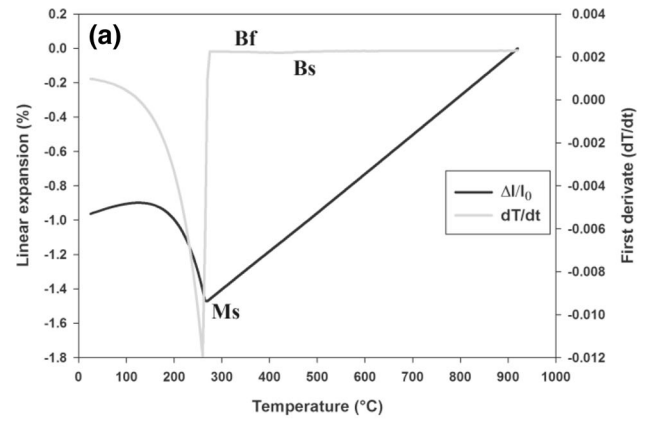


**Fig. 5** Linear expansion and first derivative of temperature for a continuous cooling rate of 30 °C/s; and 3 AGS, **a** 8, **b** 9 and **c** 10 ASTM; martensite and bainite transformation are indicated in the figure

corresponding latent heat. The HTC is defined as the ratio of the heat flux divided by the temperature difference between surface and oil. Below 280 °C heat flux increases but temperature difference becomes smaller. Then HTC recovers to reach a maximum at 200 °C. After this point, the rate of release of the latent heat starts to decrease, and so is HTC. Clearly the shape of this drop in the HTC curve depends at least on the properties of both, the oil and the steel.

### 3.2 Phase Transformation Kinetics

The sample has been austenitized at 920 °C for 520 s, for obtaining an austenite grain size of 22 μm representing an austenitic grain size (ASTM 8). Figure 4 shows the complete TTT diagram where the start and end of the transformation of pearlite and bainite is presented for the SAE 5160 steel with an austenitic grain size of (AGS 8). The results obtained for this figure have been calculated using

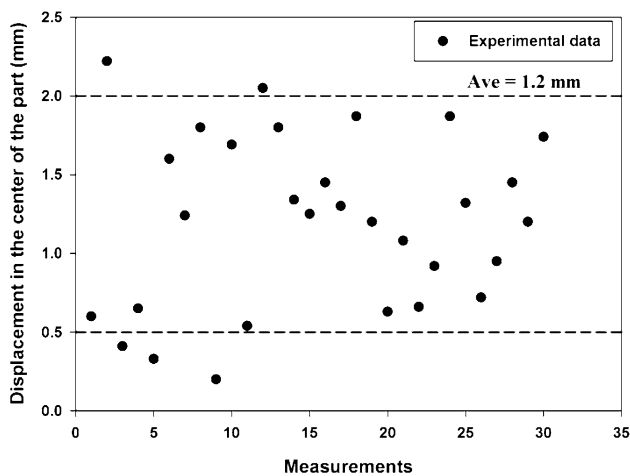


Fig. 6 Experimental data for displacement in the central part, showing an average for 30 measured parts

the software JMatPro and has been validated through quench dilatometry studies. Also, as expected, a small AGS of 9 and 10 reduces the time and critical cooling rate required to avoid bainite formation.

A typical example of these dilatometry studies is presented in Fig. 5. The martensite linear expansion is clearly found to start at approximately 270 °C and with an approximate value of 0.25 %. Bainite formation can be detected by analyzing the temperature gradient plot also shown in Fig. 5, showing a change in the linear expansion at about 500 °C, and is related to the initiation of the bainite transformation ( $B_s$ ). It can be seen that as the AGS decreases, the bainite phase volume fraction increases as well. Bainite formation has an effect on  $M_s$  temperature, through the compositional changes in carbon content in the untransformed austenite.

### 3.3 Effect of the Immersion Route and AGS on Macroscopic Distortion

As shown in Fig. 1, quenching along the Y axis has been defined as the horizontal route, while dipping along the Z axis has been termed as the vertical route. Thirty samples have been quenched in the vertical direction and the displacement at the center of the part (measured from the extremes) has been measured using a coordinate measuring machine. The results are shown in Fig. 6. It can be seen that the average measurement is approximately 1.2 mm.

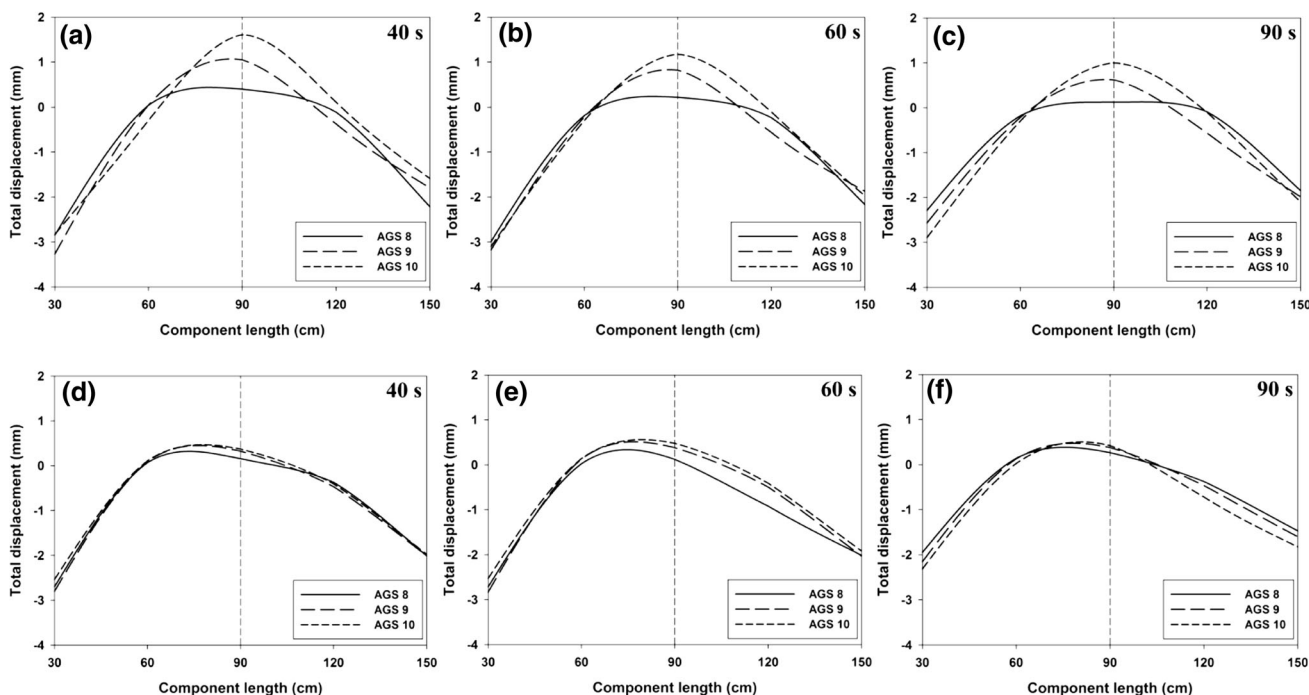
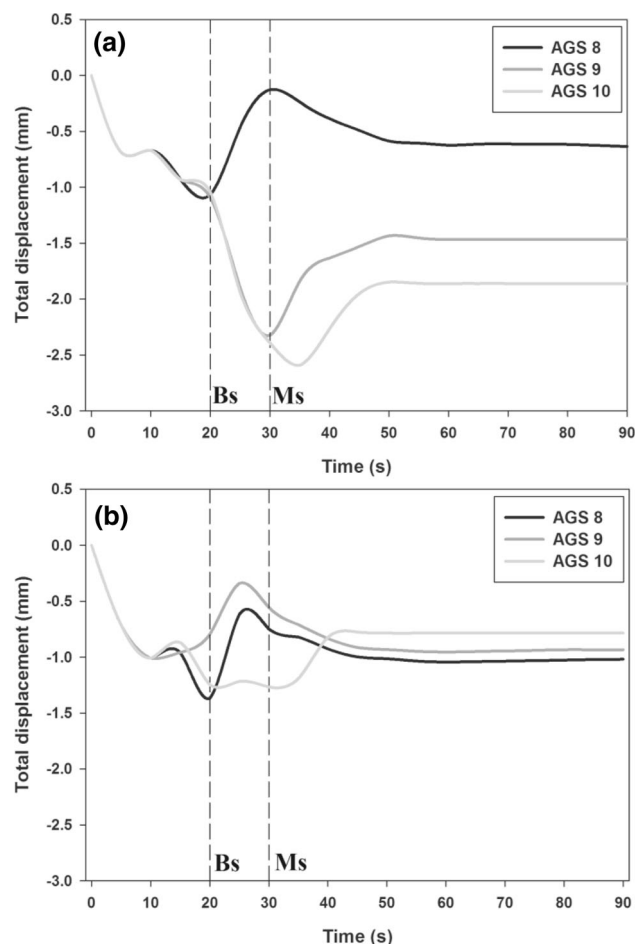


Fig. 7 Calculated total displacement along components considering three austenitic grain sizes for vertical quenching route at a 40 s, b 60 s and c 90 s; and horizontal quenching route at d 40 s, e 60 s and f 90 s



**Fig. 8** Variation of calculated average total displacement with time for **a** vertical and **b** horizontal directions and three different austenitic grain sizes

The numerical simulation considered 3 AGS (i.e., 8, 9 and 10 ASTM, 22, 16 and 11  $\mu\text{m}$ , respectively). As described previously, HTC as a function of surface temperature has been set as boundary condition to calculate the thermal evolution shown in Fig. 2.

Total displacement along the component has been calculated for the 3 AGS and plotted at 40, 60 and 90 s of quenching time. Figures 7a through c show displacement along the vertical direction, while Fig. 7d through f show the simulated displacement along the horizontal direction. The distortion in the central region is approximately 2 mm, which is comparable in magnitude to the average value found in the measurements shown in Fig. 6. It can be seen that there are important differences in displacement between the two immersion routes during the analyzed times. During the initial quenching process, there is a significant increase in displacement due to thermal contraction. However, by the end of processing, displacement arising from martensite transformation becomes more apparent. Comparing Fig. 7c, f, it can be seen that the horizontal immersion routes yield

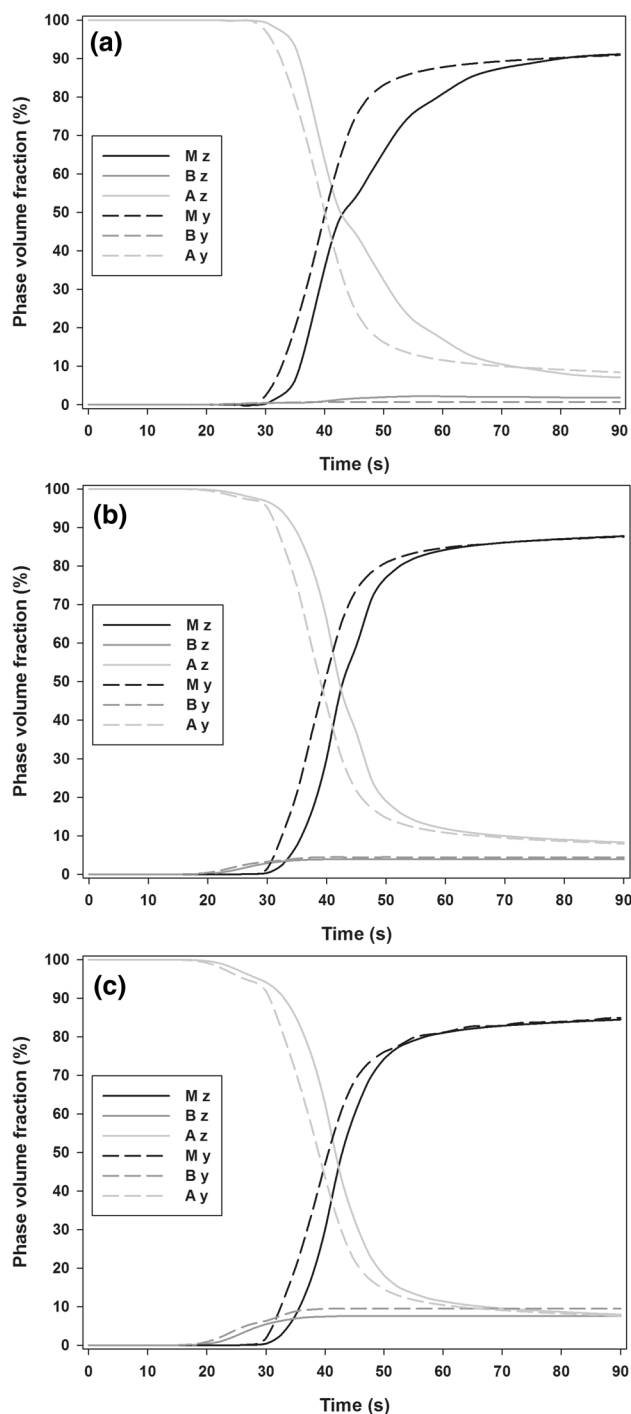


**Fig. 9** Calculated phase volume fraction evolution for both immersion routes and three different austenitic grain sizes: **a** 8, **b** 9 and **c** 10 ASTM. M, B and A stand for martensite, bainite and austenite respectively, while “y” indicates horizontal and “z” vertical routes

less displacement along the component than the vertical route for an AGS of 8 ASTM.

This may be attributed to the differences in cooling, since the vertical route may generate two martensite transformation fronts moving against each other. Once



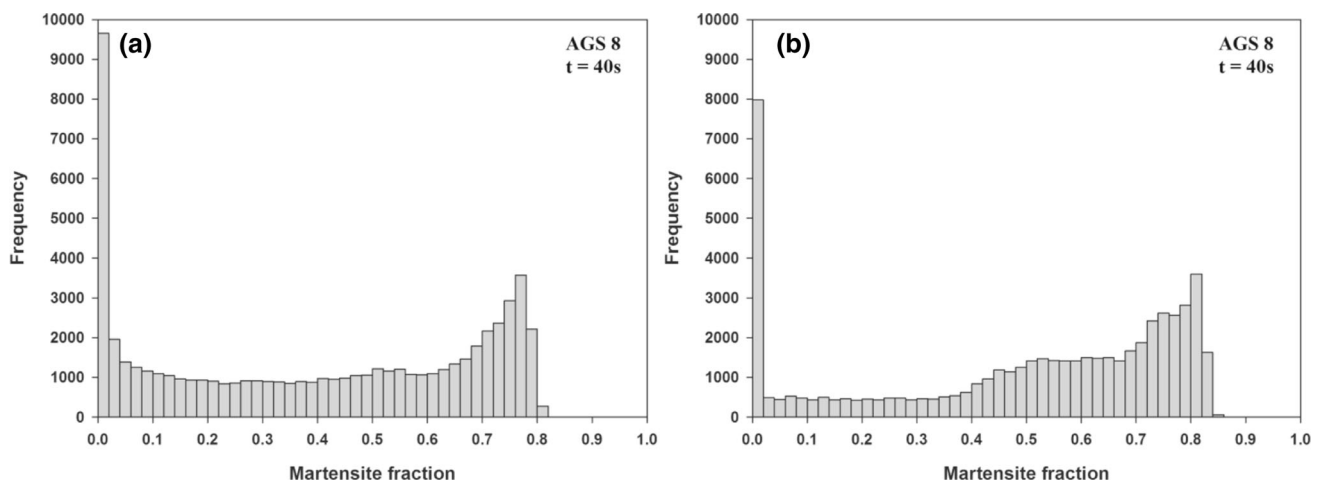


**Fig. 10** Histograms of the martensite volume fraction at the mesh nodes for **a** vertical immersion and **b** horizontal immersion, quenching time was 40 s

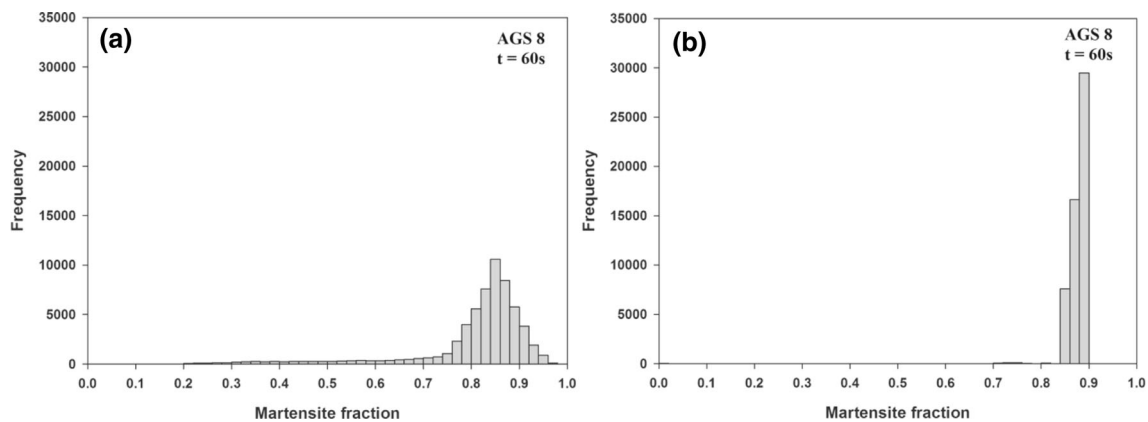


**Fig. 11** Histograms of the martensite volume fraction at the mesh nodes for **a** vertical immersion and **b** horizontal immersion, quenching time was 60 s

these fronts meet at the central part of the component, distortion may be exacerbated. Additionally, the horizontal immersion route appears to be less sensitive to the initial AGS, since there are no important differences between the 3 analyzed AGS in this route, compared to the vertical one.

In order to further analyze these phenomena, calculated total displacement has been averaged from each element value and plotted against time. This is shown in Fig. 8. It is important to remember that the plots shown in Fig. 8 are depicting average displacement, as opposed to the ones shown in Fig. 6, which show displacement along a line parallel to the component X-axis. It can be seen that most of displacement occurs in the first seconds of immersion due to thermal contraction.

There are important differences in the displacement between the 3 AGS and immersion routes. As seen in Fig. 8a, smaller AGS leads to more distortion, while AGS of 8 ASTM significantly reduces total average displacement in

the vertical immersion route. This result is in good agreement with the displacement along the component presented in Fig. 7a–c. Figure 8b shows that, average total displacement is significantly reduced, regardless of the initial AGS. It can also be seen that the displacement due to the thermal stress is also considerably reduced.

The vertical dotted lines appearing in Fig. 8 correspond to bainite start and martensite start times as calculated from the phase volume fraction evolution for the 3 different AGS shown in Fig. 9. The most important difference between the 3 AGS is bainite formation due to the TTT bainite nose shifting. Bainite formation, in turn, reduces the remaining austenite volume fraction, yielding less martensite after quenching in deterioration of the component’s hardness. By comparing Figs. 8 and 9 it can be seen why there are only minor changes in total average displacement after 60 s, since approximately 80 % of martensite has already formed at that time.

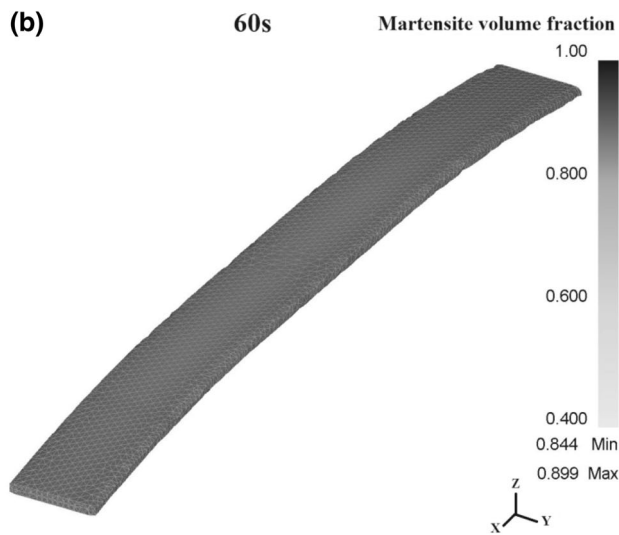
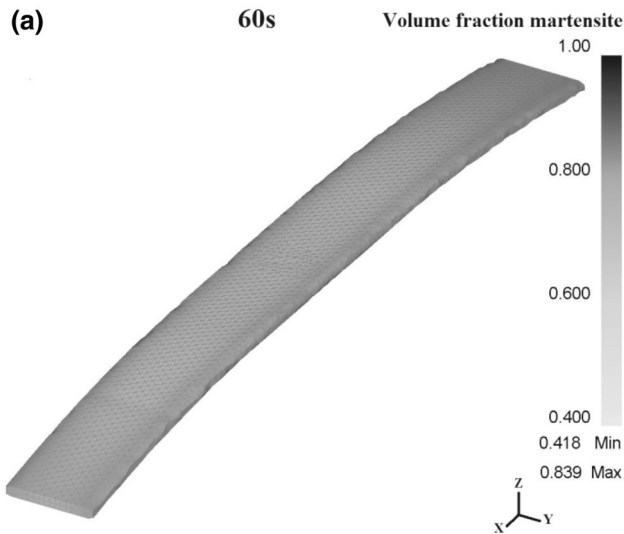


**Fig. 12** A comparison of the martensite volume fraction in the simulated component for the **a** vertical and **b** horizontal immersion routes after a quenching time of 60 s

### 3.4 Evolution of Martensite Volume Fraction and Hardness

In addition to the previously described martensite transformation front behavior, there are other important cooling differences between the immersion routes. The martensite volume fraction for each element has been calculated using the built-in Deform 3D post-processor. The phase volume fraction histograms are calculated from these results and are shown in Figs. 10 and 11 for 40 and 60 s of quenching, respectively. These histograms have been used to analyze scatter in the martensite transformation. The results demonstrate that there are no major differences between the two immersion routes after 40 s and a large fraction of

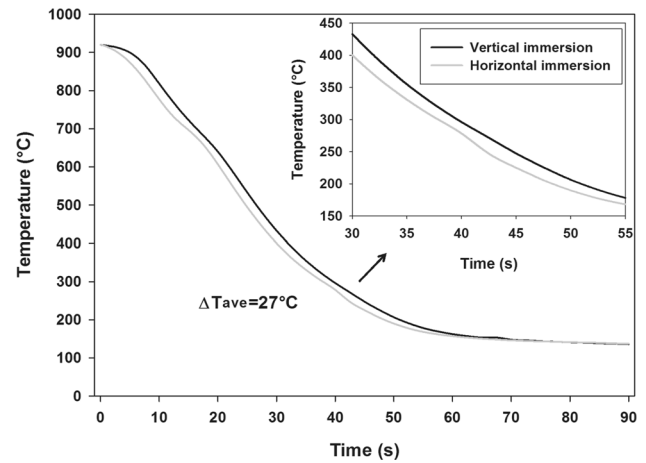


**Fig. 13** Comparison between calculated temperature changes against time for both vertical and horizontal immersion routes

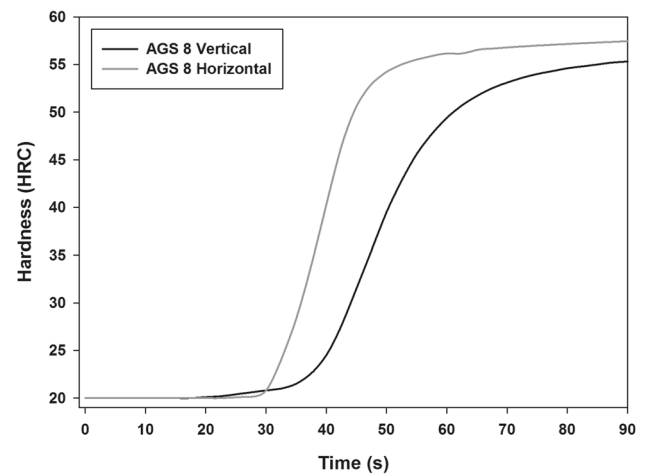


**Fig. 14** Comparison between the immersion route and result of hardness calculated for AISI 5160 steel and austenitic grain size ASTM 8

elements does not begin the austenite transformation. In contrast, Fig. 11 shows that after 60 s, there are important differences in the martensite volume fraction distribution between the two immersion routes. The histogram for the vertical immersion route clearly shows more scatter than that for the horizontal immersion route. In the vertical case, a larger number of elements still has very low martensite volume fractions even though the distribution is centered at a martensite volume fraction of approximately 85%. However, this phenomenon does not occur for the horizontal route, which has a slender shape; therefore, the martensite transformation occurs more homogeneously. A comparison between the calculated martensite volume fractions for the two immersion routes is presented in Fig. 12.

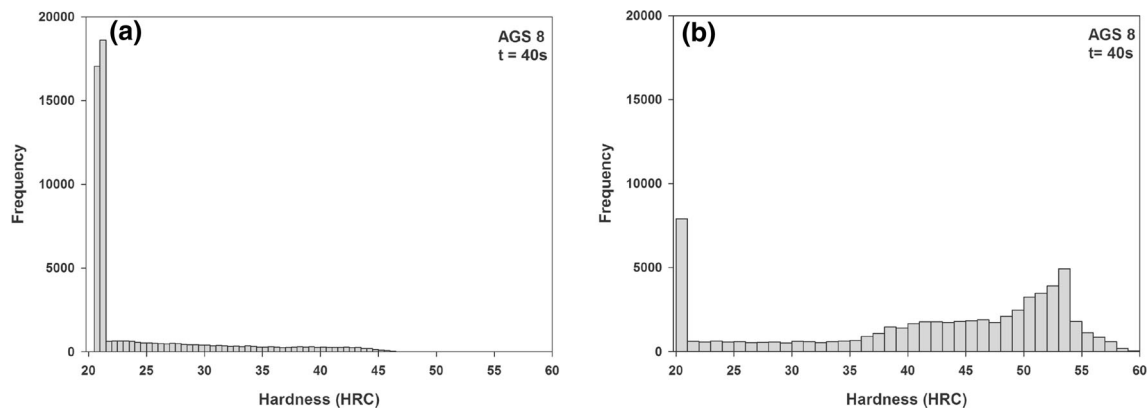
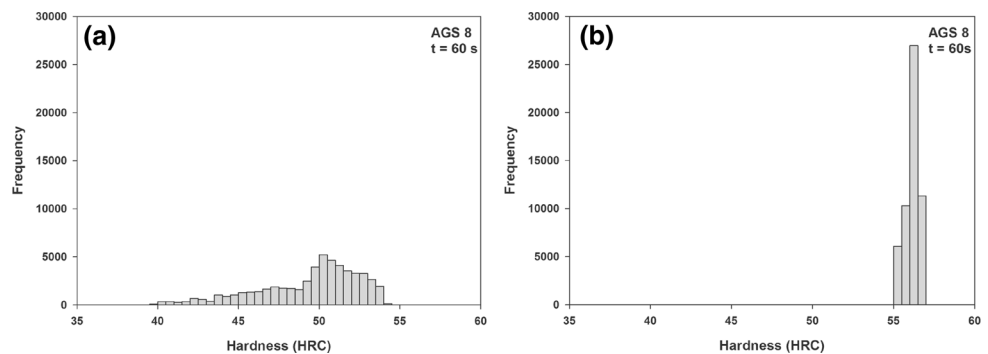


**Fig. 15** Histogram of the calculated hardness at the mesh nodes for **a** vertical immersion and **b** horizontal immersion, quenching time was 40 s

**Fig. 16** Histogram of the calculated hardness at the mesh nodes for **a** vertical immersion and **b** horizontal immersion, quenching time was 60 s



The differences in martensite volume fraction distribution between the two immersion routes can be explained by the thermal particularities of both routes. Figure 13 shows the average cooling curves for both routes. The average thermal difference is 27 °C, with the horizontal cooling route always showing the coolest temperature. This thermal difference appears to be even slightly larger at approximately 40 s. Conversely, at the Ms temperature (272 °C), the difference between the routes is of approximately 4 s. This is shown in the inset of Fig. 13.

The hardness profiles SAE 5160 steel with an austenitic grain size AGS 8 ASTM and immersion along both directions using DEFORM-3D are shown in Fig. 14. The above figure clearly shows that the hardness profile for horizontal immersion route begins to change faster than the vertical direction route. In addition, horizontal immersion route reaches its maximum hardness in a shorter time. The data obtained have been used to calculate the scattering of hardness in the full component through histograms for both the immersion routes, and are shown in Figs. 15 and 16 for 40 and 60 s of quenching, respectively.

The results demonstrate that the distribution of hardness in the quenched component has a faster transformation in the horizontal immersion route, than in the vertical route, although in some areas hardness exceeds

50 HRC for a time of 40 s as is evident from Fig. 15b. In contrast, in Fig. 15a, the majority of elements in the component are not yet transformed because the austenite to martensite transformation has not started. This is shown more clearly in Fig. 16b for horizontal immersion route for a time of 60 s, where all elements in the tempered component reaches their expected level of hardness in a shorter time than that shown in Fig. 16a, where the distribution of hardness of the material is not homogeneous. This means that the horizontal immersion route in quenching medium is more efficient for a better distribution of hardness throughout the component, which represents lower concentration of residual stress and distortion in the component.

## 4 Conclusion

A fully coupled 3D FEM model of long, curved SAE 5160 steel components that resemble leaf springs was developed in Deform 3D. The transformation kinetics was calculated using quench dilatometry; the heat transfer coefficient was calculated as a function of temperature using in-plant measurements. To achieve a proper representation of the thermal evolution in the simulated component, the heat

transfer coefficient was determined as a function of the surface temperature.

The simulation results demonstrated that the immersion route in the quenching bath had an important effect on macroscopic distortion. While thermal-related distortion seemed to be the most significant distortion source, martensite distortion also played an important role. The effects of both distortion sources appeared to be significantly reduced by choosing the horizontal immersion route in this type of long components.

Moreover, for the particular long component that was examined in this study, the best method for minimizing distortion was to quench the component starting from the long edges, since this route also minimized the initial AGS effect. It was also found that quenching from the distal ends not only increased macroscopic distortion but also increased the scatter in the martensite volume fraction and calculated hardness along the component. This enlarged scatter might also exacerbate in macroscopic distortion already started by thermal stresses because there will be volumes of fully transformed martensite that were adjacent to volumes that were yet to be transformed. These findings were particularly important for quenching system design, especially for the component type that was examined in this study.

**Acknowledgments** The authors acknowledge the Mexican Science and Technology Council (Conacyt) for supporting Mr. López-García during his Ph.D. studies at Cinvestav Saltillo. The authors especially thank San Luis Rassini's personnel, who kindly provided their facilities to perform the heat transfer coefficient measurements.

## References

- Jung M, Kang M, and Lee Y K, *Acta Mater* **60** (2012) 525.
- Lee S J, and Lee Y K, *Acta Mater* **56** (2008) 1482.
- Şimşir C, and Gür C H, *J Mater Process Technol* **207** (2008) 211.
- Da Silva A D, Pedrosa T A, Gonzalez-Mendez J L, Jiang X, Cetlin P R, and Altan T, *Mater Des* **42** (2012) 55.
- Huang D, Arimoto K, Lee K, and Lambert D, *Prediction of Quench Distortion on Steel Shaft with Keyway by Computer Simulation, Heat Treating Conference Exposition*, (2000) 1.
- Woodard P R, Chandrasekar S, and Yang H T Y, *Metall Mater Trans B* **30** (1999) 815.
- Guo Z, Saunders N, Miodownik P, and Schillé J P, *Int J Microstruct Mater Prop* **4** (2009) 187.
- Ouchi C, *ISIJ Int* **41** (2001) 542.
- Babu K, *Adv Mat Res* **488–489** (2012) 353.
- Yaakoubi M, Kchaou M, and Dammak K, *Comput Mater Sci* **68** (2013) 297.
- Barford J, and Owen W S, *Met Sci Heat Treat* **4** (1962) 359.
- Matsuzaki A, and Bhadeshia H K D H, *Mater Sci Technol* **15** (1999) 518.
- Van Bohemen S M C, *Metall Mater Trans A* **41** (2010) 285.
- Denis S, Sjöström S, and Simon A, *Metall Trans A* **18** (1987) 1203.
- Huang J, Ye X, Gu J, Chen X, and Xu Z, *Mater Sci Eng A* **532** (2012) 190.
- Denis S, Gautier E, Simon A, and Beck G, *Mater Sci Technol* **1** (1985) 805.
- Inoue T, Ju D Y, and Arimoto K, in *Proceedings of International Conference on Quenching and Control of Distortion*, ASM, Ohio, **1** (1992), p 205.
- Metals Handbook Materials Selection and Design, ASM International, Ohio **20** (1997) 774.
- Sugianto A, Narazaki M, Kogawara M, and Shirayori A, *J Mater Process Technol* **209** (2009) 4627.
- Guo Z, Saunders N, and Schillé J P, *Modelling phase transformation and materials properties critical to simulation of heat treatment distortion in steels*, Sente Software Ltd, London (2008).
- Amey C M, Huang H, and Rivera-Diaz-del-Castillo P E J, *Mater Des* **35** (2012) 66.
- Nallathambi A K, Kayamak Y, Specht E, and Bertram A, *J Mater Process Technol* **210** (2010) 204.
- Garcia-Pastor F A, Lopez-Garcia R D, Alfaro-Lopez E, and Castro-Roman M J, in *Proc of XXI International Materials Research Congress*, ASM, Mexico, **1485** (2012), p 29.
- Garcia-Pastor F A, Lopez-Garcia R D, and Castro-Roman M J, in *Proc of 5th International Conference on Thermal Process Modelling*, ASM, Ohio, (2014), p 14.
- Hasan H S, and Peet M J, *Int Commun Heat Mass Transfer* **39** (2012) 1519.
- Cheng H, Xie J, and Li J, *Comput Mater Sci* **29** (2004) 453.
- Cheng M, Cheng J, Yuan S Q, and Zhao F, *Acta Metall Sin* **10** (1997) 479.
- Huiping L, Guoqun Z, Lianfang H, and Yue M, *Measurement* **41** (2008) 676.
- Sedighi M, and McMahon C A, *J Eng Manuf* **241** (2000) 555.
- Heming C, Xieqing H, and Jianbin X, *J Mater Process Technol* **138** (2003) 399.
- Gür C H, and Tekkaya A E, *Mater Sci Eng A* **319** (2001) 164.
- Polyakov A A, *Met Sci Heat Treat* **37** (1995) 324.
- Mackerle J, *Comput Mater Sci* **27** (2003) 313.
- Gür C H, and Pan J, *Handbook of Thermal Process Modeling of Steel*, CRC Press, New York (2009).
- Şimşir C, and Gür C H, *Comput Mater Sci* **44** (2008) 588.
- Kang S H, and Im Y T, *Int J Mech Sci* **49** (2007) 423.
- Li Z, Grandhi F V, and Srinivasan R, *J Mater Process Tech* **172** (2006) 249.
- Liu C, Ju D Y, and Inoue T, *ISIJ Int* **42** (2002) 1125.
- Beck J V, *User's Manual for CONTA Program for Calculating Surface Heat Fluxes from Transient Temperatures Inside Solids, Report SAND83-7134*, Michigan State University, USA (1983) 1.
- Johnson A W, and Mehl R F, *Trans AIME* **135** (1939) 416.
- Avrami M, and Chem J, *Phys* **7** (1939) 1103.
- Koistinen D P, and Marburger R F, *Acta Metall* **7** (1939) 59.
- Scientific Forming Technologies Corporation, Columbus Ohio, DEFORM User's Manual, Version 6.1 (2007).
- Surrey Technology Center United Kingdom, Sente Software Ltd, JMatPro, Version.